Nanoscale

PAPER

Cite this: *Nanoscale*, 2016, **8**, 17022

Catalyst-free bottom-up growth of graphene nanofeatures along with molecular templates on dielectric substrates†

Misook Min,[a,b] Sohyeon Seo,*[a,c] Yeoheung Yoon,[c,d] Kyungjune Cho,[b] Sae Mi Lee,[a,c] Takhee Lee[b] and Hyoyoung Lee*[a,c,d]

Received 18th July 2016,
Accepted 7th September 2016

DOI: 10.1039/c6nr05657a

www.rsc.org/nanoscale

Synthesis of graphene nanostructures has been investigated to provide outstanding properties for various applications. Herein, we report molecular thin film-assisted growth of graphene into nanofeatures such as nanoribbons and nanoporous sheets along with a predetermined molecular orientation on dielectric substrates without metal catalysts. A Langmuir–Blodgett (LB) method was used for the formation of the molecularly patterned SiO_2 substrates with ferric stearate layers, which acted as a template for the directional growth of the polypyrrole graphene precursor. The nanofeatures of the graphene were determined by the number of ferric stearate layers (*e.g.*, nanoribbons from multiple layers and nanoporous sheets from a single layer). The graphene nanoribbons (GNRs) containing pyrrolic N enriched edges exhibited a p-type semiconducting behavior, whereas the nanoporous graphene sheets containing inhomogeneous pores and graphitic N enriched basal planes exhibited the typical electronic transport of nitrogen-doped graphene. Our approaches provide two central methods for graphene synthesis such as bottom-up and direct processes for the future development of graphene nanoelectronics.

Introduction

The structures of graphene sheets influence the electronic properties of the sheets and must be considered as a major factor in graphene-based semiconducting electronics.[1–4] Important issues are controlling the geometric size and morphology, the number of layers, and the edge terminations of grapheme, and they must be addressed. In particular, depending on the size, the electronic properties of graphene can change from metallic to semiconducting behavior.[5,6] For example, single layer graphene nanoribbons (GNRs) are a promising semiconducting material because the quantum confinement of the GNR in a one-dimensional structure may increase the band gap of graphene.[7–9] GNRs can be obtained by several different approaches such as a lithographic method,[10] an unzipping method used for carbon nanotubes,[11] a chemical exfoliation method,[7] and thermal evaporation.[12] Unfortunately, the lithographic and the chemical methods require complicated multistep fabrication processes. Even though the chemical process is simple, it is hard to control the electrical properties of the nanoribbons due to the volatile nature of the reactions; the chemical reactions can also leave a residue, resulting in decreased device performance or even device failure.[7,13] Furthermore, controlling the growth morphology of graphene to form nanofeatures such as nanoporous graphene (which behaved like a graphene nanoribbon in the electronic transport)[14] can control the band gap and improve the optical and catalytic properties of graphene, and this control is mostly performed by top-down processes.[14,15] However, considering the severe disadvantages or additional processes required by top-down methods, bottom-up synthetic methods[16–18] to control the size or shape during the graphene growth process are favourable.

In particular, direct (or bottom-up) growth of graphene nanostructures on a dielectric substrate without an additional transfer process is critically important for applications in electronic devices. In previous reports, solid carbon sources such

[a]*Department of Chemistry, Sungkyunkwan University, 2066 Seoburo, Jangan-gu, Suwon, Gyeonggi-do, Korea. E-mail: sshyeon@skku.edu, hyoyoung@skku.edu*
[b]*Department of Physics and Astronomy and Institute of Applied Physics, Seoul National University, 08826 Seoul, Korea*
[c]*Centre for Integrated Nanostructure Physics (CINAP), Institute of Basic Science (IBS), Sungkyunkwan University, 2066 Seoburo, Jangan-gu, Suwon, Gyeonggi-do, Korea*
[d]*Department of Energy and Science, Sungkyunkwan University, 2066 Seoburo, Jangan-gu, Suwon, Gyeonggi-do, Korea*

†Electronic supplementary information (ESI) available: FT-IR spectra of ferric stearate and polypyrrole films. Raman spectra of few layered GNRs as a function of temperature. Raman spectrum of few layered GNRs. AFM images of GNRs and histograms of GNRs in the width, length, and height. TEM image of a nanoporous graphene sheet. Optical images of FET devices. I_{ds}/V_{ds} characteristics of a multilayered GNRs FET. Table for Raman and XPS spectra analysis. See DOI: 10.1039/c6nr05657a

as a poly(methyl methacrylate) (PMMA) thin film[19] and organic molecular monolayers[20] were pyrolyzed to form graphene sheets on oxide substrates with metal catalysts. Furthermore, we reported the metal catalyst-free synthesis of graphene from molecular monolayers on a dielectric substrate (*e.g.*, SiO_2).[21] In spite of these efforts, however, the direct fabrication of graphene in a specific dimension still requires complicated lithographic processes. Therefore, our suggestion is to use nanostructured barrier templates to guide the growth of graphene and restrict the growth area onto selectively activated surfaces. We designed a bottom-up growth method of graphene without metal catalysts to facilely control the dimension of the solid precursors of graphene using molecular templates.

Results and discussion

Here, we synthesized template-shaped GNRs and nanoporous graphene sheets on a SiO_2 substrate without metal catalysts. We chose a heterocyclic aromatic polymer film (*e.g.*, polypyrrole, PPy) as a solid carbon source for the direct growth of graphene nanofeatures on nanoscale patterned regions (Fig. 1). A Langmuir–Blodgett (LB) method was used to prepare molecular patterns on the SiO_2 substrate using ferric stearate layers, which acted as a template for the layered growth of PPy. The thickness (or the number of layers) of the ferric stearate molecular templates is directly related to the number of two-dimensional PPy layers. Depending on the number of PPy layers, a pyrolysis reaction of PPy to graphene occurs in either ribbon or sheet shapes. Cross-linking of the PPy layers at a high temperature can form graphene sheets *via* a concerted cycloaddition reaction that is the consequence of a combined reaction between a conjugated diene (PPy) and a dienophile (PPy). Control of the growth direction requires a surface to guide the aromatized molecules to create graphene with a particular geometry. The same orientation of PPy layers can promote an aromatization reaction between the pyrrole rings responsible for preferential cycloaddition, which leads to the directional growth of graphene. As a result, two types of graphene (*i.e.*, thick-GNR and thin-graphene sheets) were synthesized depending on the thickness of the ferric stearate layers. This new method of using a surface engineered chemistry reaction of a layered conjugated polymer and the assistance of a molecular template on the SiO_2 is expected to demonstrate the preferential growth of graphene into template-shaped features.

The growth scheme of GNRs and a nanoporous graphene sheet on a SiO_2 substrate is shown in Fig. 1. The LB process produced layers of ferric stearate on the surface from a stearic acid/ferric chloride solution. The well-dried, layered

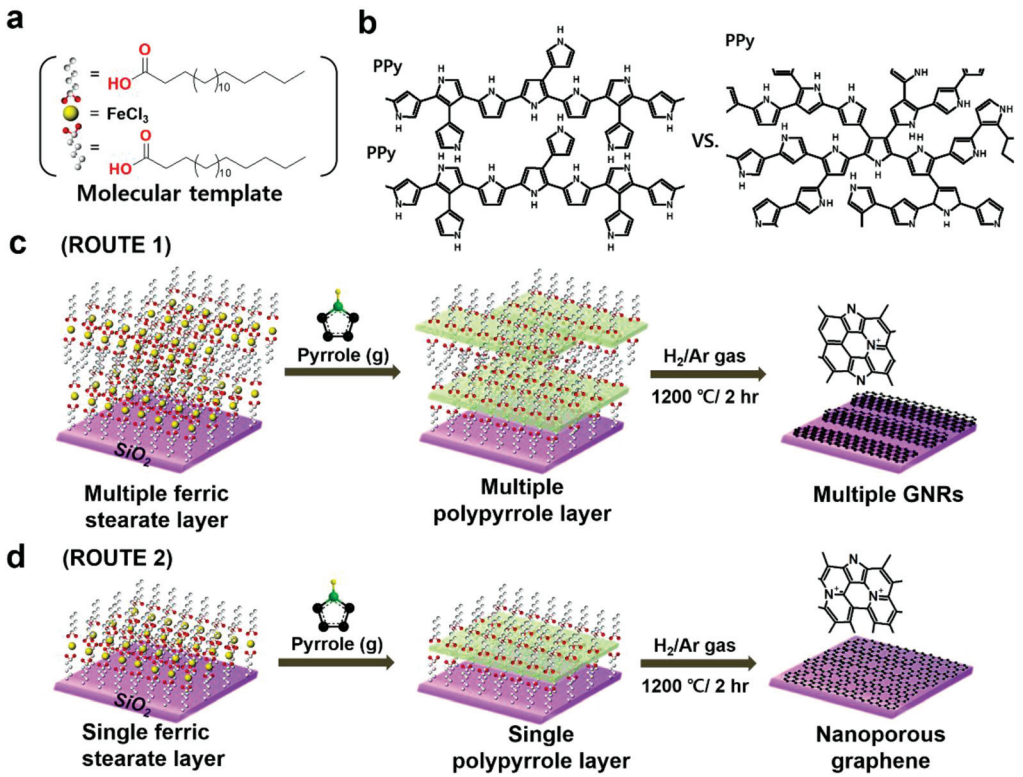

Fig. 1 Schematics of the molecular template process showing different routes for graphene synthesis. (a) Molecular template of ferric stearate. (b) Schematic structures of a multiple polypyrrole (PPy) layer *vs.* a single PPy layer. (c) ROUTE 1: a multiple ferric stearate layer acts as a template for growing a multiple PPy layer *via* the solid state reactions of pyrrole monomers (vapor). After graphitization, few layered GNRs were formed on the SiO_2 substrate. (d) ROUTE 2: a single ferric stearate layer acts as a template for growing a single PPy layer *via* the solid state reactions of pyrrole monomers (vapor). After graphitization, nanoporous graphene were formed on the SiO_2 substrate.

ferric stearate film under a hydrogen chloride (HCl) atmosphere provides a place for pyrrole monomers to polymerize into PPy. We believe that the HCl treatment for conversion of stearate ($-COO^-$) moieties into stearic acid (–COOH) moieties is to predetermine the growth direction of PPy. Thus, in ferric stearate multilayers, the conversion of stearate/Fe^{3+}/stearate to stearic acid/$FeCl_3$/stearic acid by HCl results in multilayers that are tilted and form an uneven surface (Route 1).[22] However, a single ferric stearate layer maintains a long-range two-dimensional layer even though it has defects (Route 2). Polymerization involves impregnation of a matrix material with an oxidizing salt (*i.e.*, the layer of stearic acid/$FeCl_3$/stearic acid that is the ferric stearate layer in the scheme of Fig. 1). Pyrrole vapor proceeds to the solid state polymerization reaction along a gap in the ferric stearate layers. The PPy layers can be graphitized to graphene by pyrolysis at high temperatures under low pressure H_2/Ar gas. As a result, the PPy multilayers grown in the multilayered ferric stearates would grow into layered GNRs due to coupling between the (ribbon-like) quasi one-dimensional PPy fragments in either the same or different planes, while the PPy single layer grown in the single ferric stearate layer (*i.e.*, double layered stearic acid) would form into inhomogeneous nanoporous graphene sheets mainly due to a limited carbon source of the PPy molecules in the same plane (or a lateral growth). In this process, the role of the molecular template of the ferric stearate layers is to provide places for PPy (as a precursor of graphene) to grow into the gap between the stearic acid layers where oxidizing salts (ferric chloride) for polymerization of pyrrole monomers are trapped. Thus, multiple ferric stearate layers can provide multilayered places for the growth of PPy. The formation of PPy layers or fragments on the molecular template determined the features of GNRs and nanoporous graphene.

The quality of the stearic acid and PPy layers was investigated using optical microscopy (OM), atomic force microscopy (AFM), Fourier transform infrared spectroscopy (FT-IR) and X-ray photoelectron spectroscopy (XPS). In Fig. 2a and b, the OM image shows that the LB film of ferric stearate was uniformly deposited in a large area. This area was formed by spreading a $CHCl_3$ solution of stearic acid (0.36 mM) onto water containing $FeCl_3$ (1.4×10^{-5} M).[23] The AFM image shows a single layer ferric stearate film (~5.0 nm thick) LB-deposited on a substrate. The thickness of the ferric stearate layer can be controlled by the amount of stearic acid solution, which is associated with the number of PPy layers. The white spots on the sample surface in Fig. 2b are supposed to be the residuals of stearic acid over-layered during a preparation process of LB films of ferric stearate. These stearic acid particles were eliminated during thermal annealing at high temperatures and did not affect the formation of our graphene. FT-IR spectra (Fig. S1a and S1b in the ESI†) of the ferric stearate and synthesized PPy layers show typical vibration modes for each functional group (*e.g.*, C═O and C–N), which confirm the formation of each layer. Furthermore, AFM images of polypyrrole (PPy) films grown in either single or multiple ferric stearate layers revealed that the morphology of the PPy films can predetermine the feature of synthesized graphene. A single PPy film (Fig. 2c) has lots of defects that are supposed to become holes in nanoporous graphene sheets, and a multiple PPy film (Fig. 2d) forms strips with different heights that convert to graphene nanoribbons. As the height of the defects is excluded, the single PPy film looks even in height, while the multiple PPy film exhibits two different heights in morphology (Fig. S1c and S1d in the ESI†). The high resolution C 1s spectrum (Fig. 2e) of PPy can be assigned to peaks representing sp^2 C═C (284.4 eV), sp^3 C–C (285.4 eV), and additional peaks such as C–O (286.8 eV) and $C{=}N^+$ (288.6 eV) associated with the presence of side chains, interchain links and chain terminations of PPy. Also, an N 1s spectrum (Fig. 2f) can be assigned as a neutral pyrrolic N (399.8 eV) and charged pyrrolic N (401.8 eV).[24,25] From the wide scan XPS spectrum (Fig. S1e in the ESI†), a strong O 1s peak (533.05 eV)[26] from the SiO_2 substrate was also observed. However, the Fe 2p peak was not observed in the PPy films (Fig. S1f in the ESI†), indicating that Fe atoms incorporated between the stearic acid layers are removed during the polymerization of pyrrole molecules. Also, the Fe 2p peak was not observed in the GNRs after graphitization (Fig. S2 in the ESI†). A further graphitization process was then conducted in the absence of metal catalysts.[27]

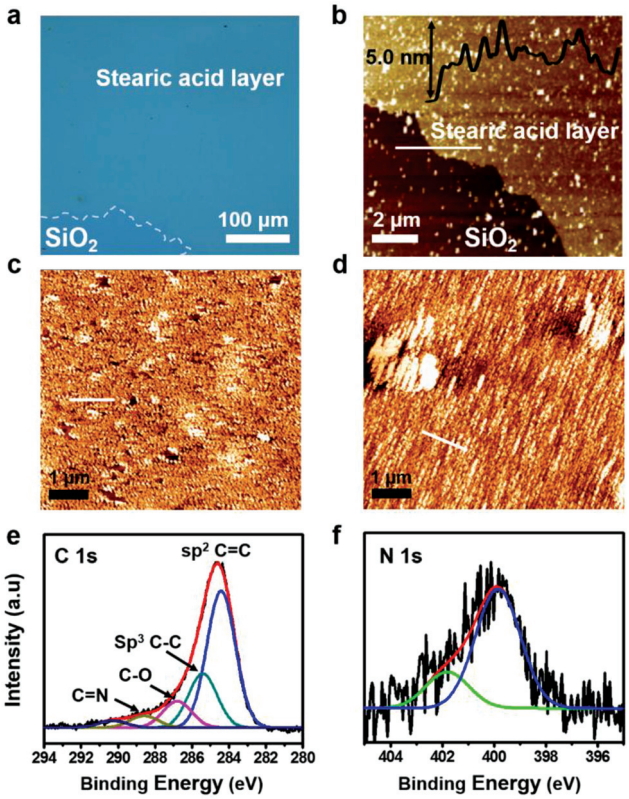

Fig. 2 (a) Optical microscopy (OM) image and (b) atomic force microscopy (AFM) image of stearic acid layers. AFM images of (c) a single PPy layer and (d) a multiple PPy layer. X-ray photoelectron spectroscopy (XPS) spectra of (e) C 1s and (f) N 1s of a PPy film.

Different pyrolysis temperatures were used to understand the growth of graphene from the multiple PPy layers (Fig. 3a). As the temperature increased from 900 to 1050 and 1200 °C, two main peaks representative of in-plane vibrational modes (the G peak at 1583–1588 cm^{-1} and the 2D peak at 2696–2719 cm^{-1}) and one disorder peak (the D peak at 1348–1359 cm^{-1}) were observed. As the temperature increased, the G and 2D peaks were significantly sharpened. In particular, at >1000 °C, the pyrolysis annealing time also affected the quality of the graphene, and a longer annealing time resulted in a better quality (Fig. S3 in the ESI†). At 1050 °C, the G peak is clearly separated from the D peak after 4 hours of annealing compared to the case of 2 hours of annealing. For single-layer graphene, the 2D peak is a single peak with a full-width at a half-maximum (FWHM) of ~30 cm^{-1}.[28] Thus, the FWHM of 2D peaks was used to confirm the number of graphene layers.[29,30] Also, single-layer graphene can be identified by the peak intensity ratio (I_{2D}/I_G) of the 2D and G peaks, which is greater than or equal to 2 in defect-free, single-layer graphene.[31] In our results, at 1200 °C, the I_{2D}/I_G intensity ratio was 0.7, and the FWHM of the 2D peak was 75 cm^{-1} (Fig. S4a in the ESI†), indicating that the synthesized graphene is probably a multilayer with defects and that the number of graphene layers is about 4 layers. As shown in Fig. S4c (in the ESI†), the plots of the peak positions in the Raman spectra taken from five places (Fig. S4b in the ESI†) exhibit the D, G, and 2D peaks at 1357 ± 2.5, 1581.6 ± 1.3, and 2715.6 ± 3.4 cm^{-1}, respectively. The D and 2D peak positions are dependent on the laser excitation energy,[29] while the G peak position shifts to lower wavenumbers[32] as the number of layers increases. Thus, the relatively small shifts in the D peak positions compared to the others indicate that changes in the thickness of the GNR in an overall area should be small. In Fig. 3a, the D peak (~1359 cm^{-1}) at 1200 °C was present at a relatively small level, indicating the presence of a few sp^3 carbon atoms or defects. Furthermore, the I_D/I_G ratio is used to evaluate the quality of graphene including GNRs;[33–35] the smaller ratio, the better the quality. At 1200 °C, the average value of the I_D/I_G ratio is about 0.53 for GNRs from a multiple PPy layer and 0.87 for nanoporous graphene sheets from a single PPy layer, indicating that the defect density on the GNRs is relatively low.[11] Also, the G peak for thicker GNRs is located at lower wavenumber than that of the G peak for the thinner nanoporous graphene sheet. With regard to graphene features (or thickness of ferric stearate layers or thickness of PPy films), Raman analysis results are summarized in Table S1 (in the ESI†).

A high-resolution transmittance electron microscopy (HR-TEM) image (Fig. 3b) of the as-grown graphene and the associated selected area electron diffraction (SAED) pattern (Fig. 3c) showed few layered graphene with a clear hexagonal lattice.[19,33,36] Each spot in the hexagonal pattern can be separated into small spots in few layered graphene because stacking faults occur between layers.[37,38] Thus, the bright and tailed spots in Fig. 3c indicated by the yellow circles come from multi-stacked graphene. The HR-TEM image indicates that the graphene had 4 layers (indicated with a yellow box) on average. Synthesis of few layered GNRs was confirmed with the narrow and long strips in the OM image and the layered structure in the HR-TEM image. Based on these microscopic images and the chemical information, the graphitization of multilayered PPy films trapped in stearic layers resulted in the direct growth of crystal-structured GNRs on SiO_2 substrates.

The XPS spectra of GNRs as a function of temperature confirm the structural progress of the graphene synthesis (Fig. 4). The sp^2 C=C (related to the C=C bonding in graphite) and the sp^3 C–C are assigned at 284.1–284.4 eV and 285.1–285.4 eV, respectively.[39,40] Small peaks are located at 286–290 eV for C–O, C=N^+, and C=O bonds.[19,41] At tempera-

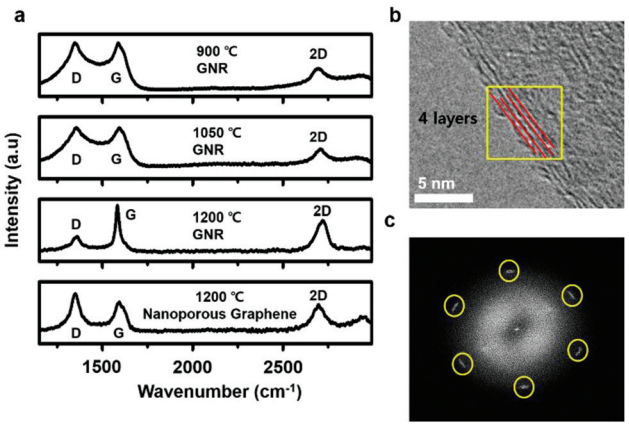

Fig. 3 (a) Raman spectrum of graphene nanoribbons (GNRs) synthesized by a new process *via* graphitization of multiple PPy layers as a function of temperature (at 900 °C, 1050 °C, and 1200 °C), and nanoporous graphene synthesized *via* graphitization of a single PPy layer at 1200 °C. (b) Transmittance electron microscopy (TEM) image and (c) selected area electron diffraction (SAED) pattern from a yellow square in (b) for the GNR synthesized at 1200 °C. The yellow circles indicate spots in the hexagonal pattern.

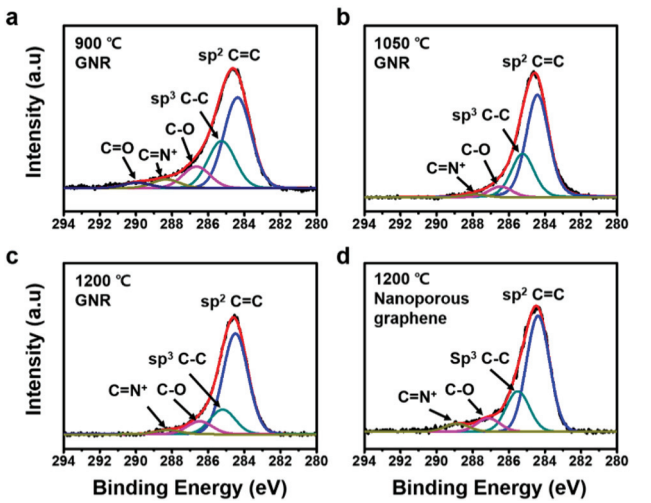

Fig. 4 (a) XPS spectra of C 1s of (a)–(c) GNRs as a function of temperature (from 900 °C to 1050 °C and 1200 °C) and (d) nanoporous graphene at 1200 °C.

tures over 1000 °C, the C═O peak disappeared, and the intensity of the functionalized peaks located at 286–290 eV decreased significantly. The peak intensity of sp^2 C═C bonding of 52.3% and 64.9% at 900 °C and 1050 °C, respectively, increased to 71.1% at 1200 °C, while the sp^3 C–C intensity of 27.1% and 27.6% at 900 °C and 1050 °C, respectively, decreased to 17.4% at 1200 °C. These XPS spectra also revealed that the 1200 °C graphitization process allowed for the formation of high quality GNRs. Thus, the bonding ratios of sp^2/sp^3 increased from 1.9/1 to 2.4/1 and 4.1/1 as the pyrolysis temperature increased from 900 °C to 1050 °C and 1200 °C. Moreover, at 1200 °C, the XPS C 1s spectrum of a nanoporous graphene sheet had a peak intensity for the sp^2 C═C bonding of 65.1% and the sp^3 C–C intensity of 22.8%, and the bonding ratio (sp^2/sp^3) of the sp^2 C═C and the sp^3 C–C was 2.9/1, which is smaller than that of the GNR. This is supposed to be associated with defects, which is consisted with the Raman result.

In addition to the OM image (Fig. S4b in the ESI†), the topographic (Fig. 5a) and correspondent amplitude AFM images (Fig. 5b) also confirm the growth of GNRs into a bundle with various widths up to ~200 nm from ~20 nm of individuals. The topographic AFM image of the GNRs reveals the thickness of the GNRs to be ~1.2 nm (~4 layers), which is consistent with the TEM result. As the AFM images in Fig. 2 and the corresponding line profiles in Fig. S1 (in the ESI†) show, only multiple ferric stearate layers (at least 4 layers) can induce longitudinally layered PPy to grow into GNRs. If PPy forms in two-dimensional thin sheets in less than 4 layers, the PPy cannot convert into GNRs. Thus, as a result, the growth of longitudinal PPy is a key step for the synthesis of GNRs. In this work, longitudinally grown PPy was not obtained from single-layer PPy. As shown in Fig. S5,† a large bundle of GNRs closely banded together into a belt-like shape was clearly observed. Moreover, small individual GNRs with a 20 nm width were not clearly imaged in a topographical image because of the surface roughness after high temperature treatment. The statistical distributions for the width, length, and height of GNRs are given in the histograms (Fig. S5 in the ESI†). The randomness of graphene nanoribbons in size may be improved, if we can pattern multilayers with lateral widths/lengths or control the reaction rate of the HCl gas. Two different types of graphene were also found in the scanning electron microscopy (SEM) images. One type was layered GNRs (in a bundle) (Fig. 5c), as confirmed in Fig. 3b (the HR-TEM image for the 4-layered GNR), while the other type included porous graphene nanosheets (Fig. 5d), as confirmed in Fig. S6 (in the ESI,† the HR-TEM image for single-layer graphene). Nanoporous graphene sheets were formed on monolayers of ferric stearate, and many defects or holes were observed in the graphene sheets. The surface morphology of the graphene sheets networked on the nanoscale was not homogeneous. Both types of graphenes contained nitrogen, and the content of nitrogen relative to carbon atoms was about 1.4% calculated from XPS spectra, which indicated that nitrogen doping in graphene occurred during the recombination of graphene precursors (*e.g.*, PPy) under high temperatures.[41] Two main peaks representing pyrrolic N (at 399.9–400.3 eV) and graphitic N (at 400.7–401.7 eV) were observed in the high resolution N 1s spectra of graphene (either nanoribbons or nanoporous sheets). The ratios of pyrrolic N to graphitic N for GNRs were >60% (*i.e.*, pyrrolic N enriched graphene), while those for nanoporous graphene sheets were <40% (*i.e.*, graphitic N enriched graphene). Raman spectroscopy results suggested that the GNRs had fewer defects. Thus, the GNRs presumably had pyrrolic-N edge terminations. In addition, pyridinic N (at 398.5–398.7 eV) in nanoporous graphene was presumably located in either the pores or edges as expected from the XPS of the porous graphene doped with nitrogen atoms.[42] With regard to graphene features (or thickness of ferric stearate layers or thickness of PPy films), XPS analysis results were summarized in Table S1 (in the ESI†).

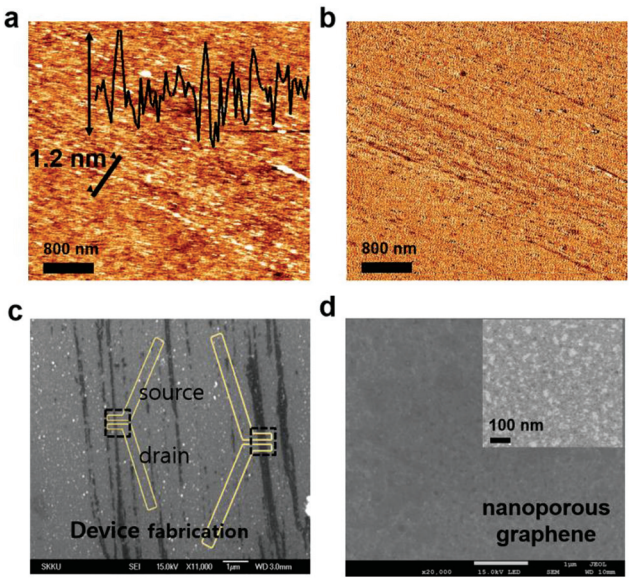

Fig. 5 (a), (b) AFM topographical image of a bundle of GNRs and the correspondent amplitude image, respectively. (c) FE-SEM image of grown GNRs and schematics (yellow drawings) for a device fabrication with electrode patterns on the selected GNRs; black dotted boxes are the channel areas. (d) FE-SEM image of nanoporous graphene (inset: a zoomed-in image). Graphene was synthesized at 1200 °C from PPy grown in molecular templates.

Finally, we measured the electrical behaviors of the as-grown GNRs (in a bundle) and nanoporous graphene sheets with back-gated field effect transistors (FETs) (Fig. 6). Our FET devices were fabricated using conventional optical lithography and a shadow mask as described in the Experimental section. Fig. S7 (in the ESI†) shows the optical images of the two kinds of FET devices. The I_{ds}/V_g (I_{ds} = source–drain currents, V_g = gate voltages) transfer characteristics of the few layered GNRs FET (Fig. 6a) exhibited a p-type semiconducting transport behavior at a source–drain voltage (V_{ds}) = 0.5 V, which is expected for pyrrolic N-doped graphene.[43,44] In the I_{ds}/V_{ds} characteristic curve at V_g = 0 V, the few layered GNRs FET showed a nonlinear transport behavior (Fig. 6b), and the

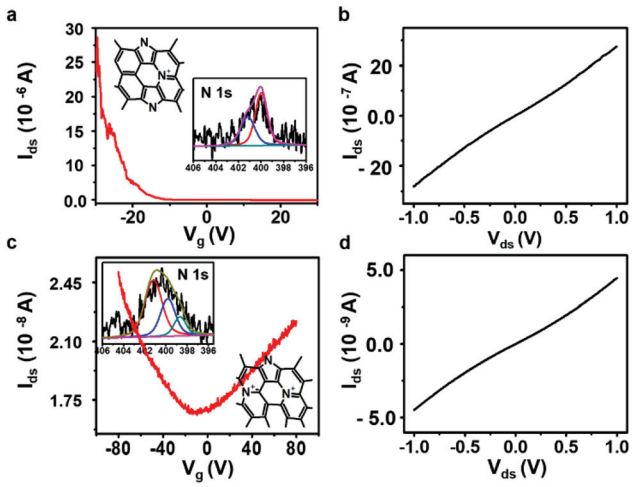

Fig. 6 For the few layered (a bundle of) GNRs FET: (a) I_{ds}/V_g transfer characteristics at a source–drain voltage (V_{ds}) = 0.5 V with a gate voltage (V_g) scan. Inset: N 1s XPS spectrum (b) I_{ds}/V_{ds} characteristics at V_g = 0 V. For the nanoporous graphene FET: (c) I_{ds}/V_g transfer characteristics at a source–drain voltage (V_{ds}) = 0.5 V with a gate voltage (V_g) scan. Inset: N 1s XPS spectrum. (d) I_{ds}/V_{ds} characteristics at V_g = 0 V. The measurement was performed at room temperature under vacuum.

multilayered (tens of layers) GNRs FET exhibited an ohmic transport behavior with metallic conductivity (146 Ω at 1 V) (Fig. S8 in the ESI†). The field effect mobility of the hole carriers (μ_h) were extracted from the slope of the curve to be μ_h = 78.7 $cm^2\ V^{-1}\ s^{-1}$ (a channel dimension: width = 670 nm and length = 4 μm) with a current ratio (I_{on}/I_{off}, on and off currents) of 200–220 at room temperature. In particular, the I_{on}/I_{off} is much larger than those (3–50) of FETs of lithographically patterned and chemically narrowed GNRs and parallel GNR arrays[45] and also (~3) of a FET of directly grown graphene micro ribbons.[12]

On the other hand, the electronic transport behavior of the nanoporous graphene sheet FET exhibited an ambipolar transfer curve of I_{ds}/V_g with a neutrality point at around −12 V (Fig. 6c). This behavior is attributed to graphitic N-doped graphene and related to the existence of irregularly patterned pores in the basal plane of graphene. The nanoporous graphene sheet FET showed an I_{ds}/V_{ds} curve and nonlinear transport behavior in Fig. 6d. Graphene nanoporous devices exhibited very low current flow, and the ratio of I_{on}/I_{off} for the on and off currents at back gate voltages of −80 V and −12 V, respectively, was measured with 1.5 at room temperature, which is similar to those (1–1.3) of lithographically patterned chemical vapor deposition graphene devices.[35,46] The field effect mobility of the hole and electron (μ_e) carriers was very low (μ_h and μ_e < 1 $cm^2\ V^{-1}\ s^{-1}$ at a channel dimension of: width = 100 μm and length = 500 μm) because of the inhomogeneous nanopores. Therefore, we can obtain the different electronic properties of graphene from the synthesis of specific graphene nanofeatures using nanostructured barrier templates: the multilayered GNRs *via* Route 1 resulted in a p-type semiconducting behavior, while the nanoporous graphene sheets with pores (or holes) *via* Route 2 resulted in electron-doping ambipolar behaviour.

Conclusion

In summary, we have shown the metal catalysts-free directional growth of graphene *via* pre-patterned PPy layers that were molecularly templated with an LB method. This novel method can also facilitate the direct growth of graphene on SiO_2 substrates. Using pyrrole vapor, the PPy single layer or multilayers were generated from the single layered or multilayered ferric stearate, respectively, and used as a carbon source for the reproducible synthesis of graphene. Depending on the deposited ferric stearate template layers, the template-shaped GNRs or nanoporous graphene sheets were synthesized. Furthermore, in near future work, we will focus on better control of the lateral growth of GNRs using layered PPy laterally patterned on substrates. The experimentally observed semiconducting nature of the multilayered GNR FET devices and the electron-doping nature of the nanoporous graphene FET devices can be used in near future nanoelectronics. We strongly expect that this directional and direct graphene growth method on the SiO_2 dielectric substrate can be easily applied to various kinds of graphene-related electronic devices without requiring any lithographic techniques or transfer processes for the graphene.

Experimental section

Materials

Pyrrole (98%) and $FeCl_3$ (97%) reagents for surface reactions were purchased from Sigma-Aldrich. Before use, the pyrrole solution was stored under nitrogen in tightly capped vials after a distillation process. H_2SO_4 and NaCl were used for producing an HCl gas on the substrates. Acetone (HPLC grade) and ethanol (HPLC grade) were used for rinsing.

Preparation of LB films

SiO_2 substrates were ultrasonically cleaned in water and acetone, followed by ethanol (10 min each), and then chemically cleaned in a solution of 3 : 1 (v/v) concentrated H_2SO_4/30% H_2O_2 for 15 min. The SiO_2 substrate was rinsed thoroughly with deionized water and ethanol and was blown-dry using nitrogen gas after each step. The cleaned SiO_2 substrate was directly used for the preparation of the LB films of ferric stearate. A stearic acid solution (0.36 mM) in chloroform was dropped in ten different places into a diluted ferric chloride (1.4×10^{-5} M) solution in water. The surface layer was then compressed until a pressure of 20 mN was reached. Finally, the ferric stearate film was formed by lifting the substrate from the LB trough.

Formation and pyrolysis of a PPy film

Concentrated sulfuric acid was added drop-wise into a NaCl solution to generate HCl gas. The LB film of the ferric stearate

layers was exposed to the HCl gas by means of a carrier N_2 gas. The substrate was then exposed to pyrrole vapor in a sealed reaction flask for 12 h under vacuum. The PPy layer film was moved into a high-vacuum furnace chamber where a 4% H_2/Ar gas of 50 sccm was introduced under low pressure. The temperature was elevated from room temperature to the target temperatures (*e.g.*, 900, 1050 and 1200 °C) for 2 h and was decreased to 30 °C for 6 h.

Fabrication of graphene FETs

(1) Conventional optical lithography was used to pattern the electrodes on the synthesized graphene nanofeatures on SiO_2 substrates. After the e-beam evaporation of the electrodes (50 nm Au/5 nm Ti), the residual photoresist was removed using the lift-off technique. (2) Without the lithographic procedures, a shadow mask (a channel width of 100 μm, a channel length of 500 μm) was used for patterning the electrodes (60 nm Au/5 nm Ti) on the synthesized graphene nanofeatures on the SiO_2 substrates.

Preparation of TEM samples

For the preparation of TEM samples, graphene grown on substrates was detached by sonication in ethanol and transferred onto a Cu grid by a drop-casting method.

Measurements

Chemical characterization of the ferric stearate and PPy layers was conducted using Fourier transform infrared spectroscopy (FT-IR, Bruker IFS-66/S) and X-ray photoelectron spectroscopy (XPS, VG Microtech ESCA 2000). Atomic force microscopy (AFM, Agilent Technologies Agilent 5500 AFM/SPM System) and optical microscopy (OM, Bimeince MIC) were used for microscopic analysis of the ferric stearate and PPy layers. The newly obtained graphene film on the SiO_2 substrate was directly characterized after it was taken from the furnace chamber using XPS, Raman spectroscopy (Renishaw, RM1000-In Via, 514 nm (2.41 eV) of the excitation energy), AFM, OM, scanning electron microscopy (SEM, JEOL JSM-7404F) and high resolution-transmittance electron microscopy (HR-TEM, JEOL JEM-2100F). HR-TEM images were obtained at 200 kV. Electrical characteristics of the devices were measured using a Keithley 4200-SCS semiconductor characterization system under vacuum conditions.

Acknowledgements

This work was supported by IBS-R011-D1.

Notes and references

1 S. Park and R. S. Ruoff, *Nat. Nanotechnol.*, 2009, **4**, 217–224.
2 J. Cai, P. Ruffieux, R. Jaafar, M. Bieri, T. Braun, S. Blankenburg, M. Muoth, A. P. Seitsonen, M. Saleh, X. Feng, K. Mullen and R. Fasel, *Nature*, 2010, **466**, 470–473.
3 X. Li, W. Cai, J. An, S. Kim, J. Nah, D. Yang, R. Piner, A. Velamakanni, I. Jung, E. Tutuc, S. K. Banerjee, L. Colombo and R. S. Ruoff, *Science*, 2009, **324**, 1312–1314.
4 A. C. Ferrari, F. Bonaccorso, V. Fal'ko, K. S. Novoselov, S. Roche, P. Boggild, S. Borini, F. H. L. Koppens, V. Palermo, N. Pugno, J. A. Garrido, R. Sordan, A. Bianco, L. Ballerini, M. Prato, E. Lidorikis, J. Kivioja, C. Marinelli, T. Ryhanen, A. Morpurgo, J. N. Coleman, V. Nicolosi, L. Colombo, A. Fert, M. Garcia-Hernandez, A. Bachtold, G. F. Schneider, F. Guinea, C. Dekker, M. Barbone, Z. Sun, C. Galiotis, A. N. Grigorenko, G. Konstantatos, A. Kis, M. Katsnelson, L. Vandersypen, A. Loiseau, V. Morandi, D. Neumaier, E. Treossi, V. Pellegrini, M. Polini, A. Tredicucci, G. M. Williams, B. Hee Hong, J.-H. Ahn, J. Min Kim, H. Zirath, B. J. van Wees, H. van der Zant, L. Occhipinti, A. Di Matteo, I. A. Kinloch, T. Seyller, E. Quesnel, X. Feng, K. Teo, N. Rupesinghe, P. Hakonen, S. R. T. Neil, Q. Tannock, T. Lofwander and J. Kinaret, *Nanoscale*, 2015, **7**, 4598–4810.
5 Y. Li, Z. Zhou, P. Shen and Z. Chen, *ACS Nano*, 2009, **3**, 1952–1958.
6 J. Hicks, A. Tejeda, A. Taleb-Ibrahimi, M. S. Nevius, F. Wang, K. Shepperd, J. Palmer, F. Bertran, P. Le Fevre, J. Kunc, W. A. de Heer, C. Berger and E. H. Conrad, *Nat. Phys.*, 2013, **9**, 49–54.
7 X. Li, X. Wang, L. Zhang, S. Lee and H. Dai, *Science*, 2008, **319**, 1229–1232.
8 T. Shimizu, J. Haruyama, D. C. Marcano, D. V. Kosinkin, J. M. Tour, K. Hirose and K. Suenaga, *Nat. Nanotechnol.*, 2011, **6**, 45–50.
9 N. Liu, K. Kim, H. Y. Jeong, P.-C. Hsu, Y. Cui and Z. Bao, *ACS Nano*, 2015, **9**, 9043–9049.
10 Z. Chen, Y.-M. Lin, M. J. Rooks and P. Avouris, *Physica E*, 2007, **40**, 228–232.
11 L. Jiao, L. Zhang, X. Wang, G. Diankov and H. Dai, *Nature*, 2009, **458**, 877–880.
12 D. Wang, H. Tian, Y. Yang, D. Xie, T.-L. Ren and Y. Zhang, *Sci. Rep.*, 2013, **3**, 1348.
13 Y.-C. Chen, D. G. de Oteyza, Z. Pedramrazi, C. Chen, F. R. Fischer and M. F. Crommie, *ACS Nano*, 2013, **7**, 6123–6128.
14 M. Kim, N. S. Safron, E. Han, M. S. Arnold and P. Gopalan, *Nano Lett.*, 2010, **10**, 1125–1131.
15 H. Tanaka, R. Arima, M. Fukumori, D. Tanaka, R. Negishi, Y. Kobayashi, S. Kasai, T. K. Yamada and T. Ogawa, *Sci. Rep.*, 2015, **5**, 12341.
16 J. Sun, Y. Chen, M. K. Priydarshi, Z. Chen, A. Bachmatiuk, Z. Zou, Z. Chen, X. Song, Y. Gao, M. H. Rümmeli, Y. Zhang and Z. Liu, *Nano Lett.*, 2015, **15**, 5846–5854.
17 Y. Chen, J. Sun, J. Gao, F. Du, Q. Han, Y. Nie, Z. Chen, A. Bachmatiuk, M. K. Priydarshi, D. Ma, X. Song, X. Wu, C. Xiong, M. H. Rümmeli, F. Ding, Y. Zhang and Z. Liu, *Adv. Mater.*, 2015, **27**, 7839–7846.
18 J. Sun, Y. Zhang and Z. Liu, *ChemNanoMat*, 2016, **2**, 9–18.

19 Z. Sun, Z. Yan, J. Yao, E. Beitler, Y. Zhu and J. M. Tour, *Nature*, 2010, **468**, 549–552.

20 H.-J. Shin, W. M. Choi, S.-M. Yoon, G. H. Han, Y. S. Woo, E. S. Kim, S. J. Chae, X.-S. Li, A. Benayad, D. D. Loc, F. Gunes, Y. H. Lee and J.-Y. Choi, *Adv. Mater.*, 2011, **23**, 4392–4397.

21 H. Jing, M. Min, S. Seo, B. Lu, Y. Yoon, S. M. Lee, E. Hwang and H. Lee, *Carbon*, 2015, **86**, 272–278.

22 R. B. Rosner and M. F. Rubner, *Chem. Mater.*, 1994, **6**, 581–586.

23 S. Ye, H. Noda, S. Morita, K. Uosaki and M. Osawa, *Langmuir*, 2003, **19**, 2238–2242.

24 D. Kowalski, A. Tighineanu and P. Schmuki, *J. Mater. Chem.*, 2011, **21**, 17909–17915.

25 L. Atanasoska, K. Naoi and W. H. Smyrl, *Chem. Mater.*, 1992, **4**, 988–994.

26 G. Hollinger, Y. Jugnet, P. Pertosa and T. Minh Duc, *Chem. Phys. Lett.*, 1975, **36**, 441–445.

27 J. Chen, Y. Wen, Y. Guo, B. Wu, L. Huang, Y. Xue, D. Geng, D. Wang, G. Yu and Y. Liu, *J. Am. Chem. Soc.*, 2011, **133**, 17548–17551.

28 D. Graf, F. Molitor, K. Ensslin, C. Stampfer, A. Jungen, C. Hierold and L. Wirtz, *Nano Lett.*, 2007, **7**, 238–242.

29 A. C. Ferrari, J. C. Meyer, V. Scardaci, C. Casiraghi, M. Lazzeri, F. Mauri, S. Piscanec, D. Jiang, K. S. Novoselov, S. Roth and A. K. Geim, *Phys. Rev. Lett.*, 2006, **97**, 187401.

30 Y. Hao, Y. Wang, L. Wang, Z. Ni, Z. Wang, R. Wang, C. K. Koo, Z. Shen and J. T. L. Thong, *Small*, 2010, **6**, 195–200.

31 B. Sensale-Rodriguez, R. Yan, M. M. Kelly, T. Fang, K. Tahy, W. S. Hwang, D. Jena, L. Liu and H. G. Xing, *Nat. Commun.*, 2012, **3**, 780.

32 A. Gupta, G. Chen, P. Joshi, S. Tadigadapa and P. C. Eklund, *Nano Lett.*, 2006, **6**, 2667–2673.

33 L. Jiao, X. Wang, G. Diankov, H. Wang and H. Dai, *Nat. Nanotechnol.*, 2010, **5**, 321–325.

34 S. Ryu, J. Maultzsch, M. Y. Han, P. Kim and L. E. Brus, *ACS Nano*, 2011, **5**, 4123–4130.

35 A. Reina, X. Jia, J. Ho, D. Nezich, H. Son, V. Bulovic, M. S. Dresselhaus and J. Kong, *Nano Lett.*, 2009, **9**, 30–35.

36 J. Sun, T. Gao, X. Song, Y. Zhao, Y. Lin, H. Wang, D. Ma, Y. Chen, W. Xiang, J. Wang, Y. Zhang and Z. Liu, *J. Am. Chem. Soc.*, 2014, **136**, 6574–6577.

37 A. W. Robertson and J. H. Warner, *Nano Lett.*, 2011, **11**, 1182–1189.

38 J. Campos-Delgado, J. M. Romo-Herrera, X. Jia, D. A. Cullen, H. Muramatsu, Y. A. Kim, T. Hayashi, Z. Ren, D. J. Smith, Y. Okuno, T. Ohba, H. Kanoh, K. Kaneko, M. Endo, H. Terrones, M. S. Dresselhaus and M. Terrones, *Nano Lett.*, 2008, **8**, 2773–2778.

39 M. A. Fanton, J. A. Robinson, C. Puls, Y. Liu, M. J. Hollander, B. E. Weiland, M. LaBella, K. Trumbull, R. Kasarda, C. Howsare, J. Stitt and D. W. Snyder, *ACS Nano*, 2011, **5**, 8062–8069.

40 A. N. Sokolov, F. L. Yap, N. Liu, K. Kim, L. Ci, O. B. Johnson, H. Wang, M. Vosgueritchian, A. L. Koh, J. Chen, J. Park and Z. Bao, *Nat. Commun.*, 2013, **4**, 2402.

41 D. Wei, Y. Liu, Y. Wang, H. Zhang, L. Huang and G. Yu, *Nano Lett.*, 2009, **9**, 1752–1758.

42 F. Zheng, Y. Yang and Q. Chen, *Nat. Commun.*, 2014, **5**, 5261.

43 Y.-F. Lu, S.-T. Lo, J.-C. Lin, W. Zhang, J.-Y. Lu, F.-H. Liu, C.-M. Tseng, Y.-H. Lee, C.-T. Liang and L.-J. Li, *ACS Nano*, 2013, **7**, 6522–6532.

44 H. S. Kim, H. S. Kim, S. S. Kim and Y.-H. Kim, *Nanoscale*, 2014, **6**, 14911–14918.

45 X. Wang and H. Dai, *Nat. Chem.*, 2010, **2**, 661–665.

46 Z. Yan, Z. Peng, Z. Sun, J. Yao, Y. Zhu, Z. Liu, P. M. Ajayan and J. M. Tour, *ACS Nano*, 2011, **5**, 8187–8192.